Inorganic Chemistry

pubs.acs.org/IC Article

Structural and Microstructural Characterization of Fission Product Phases in MOX Nuclear Fuel for Fast Neutron Reactors

Rafael Caprani, Philippe Martin,* Damien Prieur, Julien Martinez, Florent Lebreton, Elena F. Bazarkina, Kristina O. Kvashnina, Denis Menut, Méghan Alibert, Stéphanie Lecoq, and Nicolas Clavier

Cite This: *Inorg. Chem.* 2026, 65, 3255−3269

Read Online

ACCESS | Metrics & More | Article Recommendations | Supporting Information

ABSTRACT: In the context of spent fuel recycling and the valorization of plutonium, (U,Pu)O_2 mixed oxides (MOX) have been developed for use in French Pressurized Water Reactors (PWR). They are also leading candidates for some GEN IV reactor concepts, such as sodium-cooled fast reactors (SFR). One of the critical challenges in the nuclear industry is the mastery of the nuclear fuel cycle, specifically plutonium multirecycling. In order to achieve this goal, it is crucial to identify the secondary phases created during irradiation. In this work, (U,Pu)O_2 MOX have been doped with 11 stable fission products (FP) (Sr, Y, La, Nd, Ce, Zr, Mo, Pd, Rh, Ru, Ba) to reproduce FP-based precipitates existing in the real spent fuel. The structural and microstructural properties of these secondary phases were characterized by coupling scanning electron microscopy-energy dispersive X-ray spectroscopy (SEM-EDS), Electron Probe MicroAnalysis (EPMA), and synchrotron techniques such as X-ray Absorption Spectroscopy (XAS) and Synchrotron Powder X-ray Diffraction (SP-XRD). This analysis highlights the relationship between the partial segregation among metallic FP (Mo, Pd, Rh, Ru) and their crystallographic structures, as well as the speciation shift of several FP induced by the addition of Ba. The synthesized SIMMOX samples present a secondary phase representative of irradiated MOX and can be used as an effective model material to study spent nuclear fuel and its reprocessing.

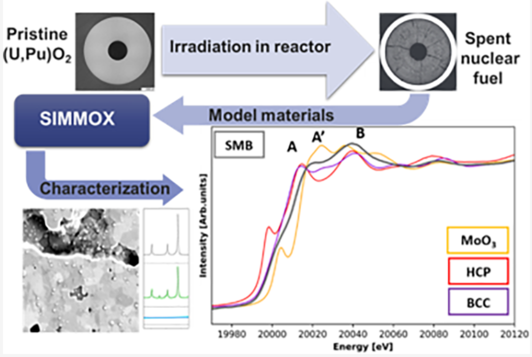

1. INTRODUCTION

Among all types of nuclear fuels, actinide oxides such as UO_2 are the most widely used and the most extensively studied. In the context of spent fuel recycling and valorization of nuclear waste, (U,Pu)O_2 mixed oxides (MOX) have been developed as an alternative fuel. MOX are currently used in several French Pressurized Water Reactors (PWR), and is a key component in the designs of various future Generation IV (GEN IV) reactors, such as sodium-cooled fast reactors (SFR).[1−3] In this context, mastering the nuclear fuel cycle is crucial, and understanding the properties of MOX under irradiation, during intermediate storage, and throughout reprocessing is of utmost importance.[1,4−11]

Studying irradiated fuel poses significant challenges due to the strict radioprotection requirements associated with such materials, which impose the use of dedicated hot cells during analysis and sample handling. Additionally, the extreme and peculiar conditions the fuel experienced, such as steep temperature gradients and a continuously evolving chemical composition as a result of the formation of fission products (FP), make this material an extremely complex system.[4,12] Fission products can be categorized into five primary families, always simultaneously present in irradiated fuel: those soluble in the (U,Pu)O_2 solid solution (rare earth elements (REE), Zr, Sr, Nb), those forming metallic inclusions sometimes referred as "white phases" (Mo, Tc, Ru, Rh, Pd), those precipitating into secondary oxide phases also known as "gray phases" (mainly Ba and Sr compounds such as $BaZrO_3$ perovskites), volatile fission products (Cs, Te, I), and fission gases (Kr, Xe). As a result, isolating the effects of specific fission products is virtually impossible.[4,13−18]

The influence of individual fission products or FP families on the properties of irradiated MOX remains unclear because only a limited number of facilities worldwide possess the capabilities to experimentally investigate these materials. To address this gap, model materials, named SIMFUEL, made of "fresh" (unirradiated) UO_2 doped with stable isotopes of fission products, have been developed.[19−24] The SIMFUEL approach, although extremely insightful, cannot correctly replicate the complex chemistry of MOX fuel due to the presence of Pu and other transuranic elements. In order to

Received: September 5, 2025
Revised: December 16, 2025
Accepted: January 13, 2026
Published: February 4, 2026

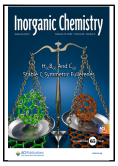

https://doi.org/10.1021/acs.inorgchem.5c04163

Table 1. Composition of the Three SIMMOX Batches S,[25] SM, and SMB, Given as Mass Fractions (wt %)[a]

	Ba	Ce	La	Mo	Nd	Pd	Rh	Ru	Sr	Y	Zr	U	Pu	Am
S[25]		0.88	0.43		2.10				0.11	0.11	1.00	61.1	21.0	0.42
SM		0.84	0.44	1.45	1.96	0.80	0.34	1.49	0.12	0.10	1.18	58.6	20.2	0.40
SMB	0.86	0.83	0.43	1.44	1.94	0.79	0.34	1.47	0.12	0.10	1.17	58.1	20.0	0.40

[a] Data for batch S are obtained through ICP-MS, while EPMA was employed for batches SM and SMB. The complement to 100% belongs to the oxygen content.

extend the SIMFUEL methodology to Pu-bearing materials, we previously developed a synthesis route for a model material called "SIMMOX",[25] focusing on understanding the interaction between the (U,Pu)O_2 matrix and six key FP that are known to incorporate into the solid solution with actinides: Ce, La, Nd, Sr, Y, and Zr.

In this work, we have expanded our focus to investigate the formation and influence of secondary phases derived from fission products, particularly the metallic (white phases) and oxide precipitates (gray phases) that characterize irradiated MOX fuel. To simplify the analysis, the volatile and gaseous fission products have been omitted, enabling us to isolate the effects of the metallic and oxide precipitates on the MOX properties and microstructure.

The speciation of fission products (FP) and their effects on the U−Pu−O system were extensively studied through a comprehensive multiscale approach combining X-ray Absorption Spectroscopy (XAS), Scanning Electron Microscopy (SEM) coupled with Energy-Dispersive Spectroscopy (EDS), and Electron Probe MicroAnalysis (EPMA). Furthermore, due to the low concentration of each individual type of FP-based secondary phase (<5 wt %), Synchrotron Powder X-ray Diffraction (SP-XRD) was performed in order to identify the crystallographic phases (i.e., space group identification and lattice parameter determination) of such inclusions. This combination of techniques allowed us to identify the FP-based secondary phases across all SIMMOX samples. Metallic phases and oxide precipitates were clearly characterized, and we also determined the oxidation states of each actinide and fission product.

2. MATERIALS AND METHODS

2.1. Safety Statement

Caution! Plutonium and Americium are strong α and γ emitters, which entail significant irradiation and internal contamination risks. All actinide-bearing materials should be handled in gloveboxes inside dedicated facilities.

2.2. Sample Synthesis and Description

We based the composition of our study on an SFR MOX fuel irradiated to 13 atom % burnup (126.2 GWd/tHMi), setting the Pu/(U + Pu) ratio at 26 wt %. This ensured consistency with the (U,Pu,FP)O_2 matrix used in our previous work.[25] Two new sample batches were synthesized for this study: one aimed at reproducing white phases through the addition of Mo, Rh, Ru, and Pd, and another designed to explore the role of Ba in forming perovskite-type phases, which are the main component of the gray phases.

The samples were synthesized following a comilling route developed in our previous work on soluble Fission Products (FP).[25] First, the actinides and the FP surrogate powders were blended together in appropriate ratios, with a 0.5 L container rotating at 24 rpm for 30 min. Ball milling was performed for 4 h, and then the powder was pressed at 450 MPa in order to obtain "green" pellets with cylindrical geometries of 6 mm diameter and 5 mm height. The pellets were sintered at 1973 K for 4 h under a flowing atmosphere of composition Ar + 4.3% H_2 + 1200 vpm H_2O.

In order to reproduce and study the precipitates of the irradiated MOX fuel, two additional batches of SIMMOX samples were synthesized. Our starting SIMMOX batch[25] is named "S" as the only FP it contains belongs to the family of the ones considered "Soluble" in the $U_{1-y}Pu_yO_2$ matrix (Ce, La, Nd, Sr, Y, Zr). The second batch has been obtained by adding to the composition S stable oxide compounds of elements known to make up the metallic precipitates (white phases), such as Mo, Pd, Rh, and Ru. This second batch has been called "SM" as it contains both Soluble and "Metallic" FP. With the same logic, the third batch has been obtained by taking the composition of SM and adding Ba as $BaCO_3$. This batch has been hence named "SMB", as it contains everything in SM with the addition of barium. Table 1 summarizes the compositions of the three SIMMOX batches, as described above. The composition of batch S has been obtained through complete dissolution and subsequent inductively coupled plasma mass spectrometry (ICP-MS) analyses.[25] Such a protocol cannot be applied to samples SM and SMB due to the refractory nature of metallic precipitates to dissolution; hence, their composition was first calculated starting from the mass of precursors and then verified by EPMA.

2.3. Sample Characterization

The whole characterization, with the exception of XAS and SP-XRD, has been carried out at the ATALANTE facility in the CEA-Marcoule site, France. All the following equipment, with the aforementioned exceptions, is partially or completely nuclearized in dedicated actinide-grade gloveboxes.

2.3.1. Optical and Electron Microscopy. The samples were first subjected to a longitudinal cut and mirror-polished. Optical imaging was performed with an optical microscope installed by Optic Peter and equipped with an objective and a camera from Olympus.

From each sample, a slice of roughly 1 mm thickness was cut and glued on an SEM aluminum sample holder with a conductive carbon adhesive tab. SEM analysis was carried out with a TESCAN MIRA3 equipped with an X-PLORE EDS detector supplied by Oxford Instruments.

The images were acquired at 20 kV, with an absorbed electron current on the stage of 1.9 nA and a spot size of 43 nm. The deconvolution of energy adjacent peaks was performed through the automatic routine proposed by AZtec software supplied by Oxford Instruments.

2.3.2. Electron Microprobe Analysis. All local composition measurements were performed through EPMA with a CAMECA SX100 equipped with a tungsten wire electron gun. The electron beam was accelerated by an electrostatic potential of 20 kV, and the current intensity was set between 50 and 200 nA. Two-dimensional (2D) maps were collected on several (1024 × 1024 or 512 × 512 μm^2) areas of the samples by stage mapping with longitudinal and transverse steps of 1 μm, a time per step of 20 ms, and without background subtraction. Quantitative measurements were also performed along several 200 μm lines with a step of 1 μm and a counting time of at least 15 s on the peak and 2 × 5 s on the background. Quantitative measurements were processed using the CAMECA Peaksight 6.5 software, applying the X-PHI correction method.[26] Detection limits were calculated using the method described by Ancey et al.[27] The reference materials and lines used were BaF_2 for Ba L_α, $CeAl_2$ for Ce L_α (with an unavoidable contribution from Ba L_β), LaB_6 for La L_α, $NdPO_4$ for Nd L_β (to avoid the contribution from Ce L_β), SrF_2 for Sr L_α, UO_2 for O K_α and U M_α, PuO_2 for Pu M_β (to avoid a contribution from U M_β),

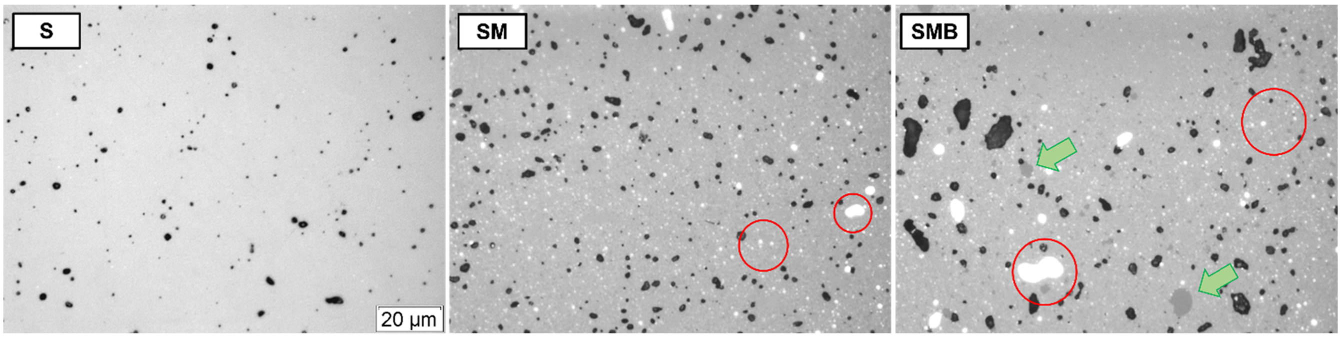

Figure 1. Comparison of optical microscopy imaging of the three SIMMOX sample compositions: S,[25] SM, and SMB. The white inclusions (red circles) represent the white phases, while the darker inclusions (green arrows) represent the gray phases. The black spots correspond to the porosities.

$(Pu_{0.92}Am_{0.08})O_2$ for Am M_α and pure metallic reference materials for Mo L_α, Pd L_β (to avoid a contribution from Rh L_β), Rh L_α (with an unavoidable contribution from Ru L_β), Ru L_α, Y L_α, and Zr L_α. All reference materials were provided by MAC (Micro-Analysis Consultants Ltd., U.K.), except for the actinide oxides, which were lab-made. The overlaps of U (M_γ) on Pu M_β and Ba (L_β) on Ce L_α were corrected using the same reference materials. All lines were measured using a pentaerythritol (PET) crystal ($2d = 0.874$ nm), except for the Y, Zr, and Sr L_α lines measured with a thallium acid phthalate (TAP) crystal ($2d = 2.575$ nm) and the O K_α line, measured with a PC1 W/Si multilayer pseudocrystal ($2d = 6.1$ nm).

2.3.3. X-ray Diffraction. Synchrotron powder XRD (SP-XRD) analyses were performed at the MARS beamline[28] of the SOLEIL synchrotron. SIMMOX samples were ground into fine powder (1−2 mg) and then diluted with amorphous SiO_2 in order to reduce their density. The powder was then confined in four layers of Kapton capillaries in order to avoid radiological dissemination at the beamline and spun into the beam during the measurement. The beam was vertically collimated and set to a size of 1000 × 300 μm^2 ($H \times V$). Its energy was calibrated using the Y K-edge (17.038 keV). The diffractograms were recorded in the Debye−Scherrer geometry with the use of a 2-dimensional Pilatus3 2M CdTe (DECTRIS AG, Switzerland) detector mounted on a motorized support allowing 2Θ trajectories. Thus, 10 images were recorded with a 2Θ step of 5°, further reduced and concatenated with PyFAI[29] and a homemade Jupyter Notebook to obtain a one-dimensional XRD diagram ranging from 1.5 to 60° 2Θ. The setup geometry was calibrated with a 660C-LaB_6 standard from NIST. Data analysis was performed using the Fullprof suite software[30] in LeBail mode.

Plutonium isotopes and Americium-241, being strong α emitters, subject Am- and Pu-bearing compounds to significant self-irradiation. This phenomenon is notably known to cause lattice parameter swelling, as documented in several studies.[31−35] Based on our isotopic composition and previously established empirical laws, the estimated self-irradiation-induced swelling is less than 1×10^{-3} Å. Given that this value is below the experimental uncertainty, it can be considered negligible.

2.3.4. X-ray Absorption Spectroscopy. X-ray Absorption Spectroscopy (XAS) data were measured at the HZDR-operated ESRF-ROBL beamline (BM20).[36,37] Data were recorded using a Si(111) double-crystal monochromator coupled with collimating and focusing Rh-coated mirrors, while the samples were held at a temperature of 15 K. XAS data were collected in transmission mode and in fluorescence mode with an electrically cooled (Cryo-Pulse 5 Plus) 18-element Ge detector (Ultra-LEGe, GUL0055, Mirion Technologies). X-ray absorption near edge structure (XANES) was collected at the following edges: U L_3-edge, Pu L_3-edge, Am L_3-edge, Sr K-edge, Y K-edge, Zr K-edge, Rh K-edge, Pd K-edge, Mo K-edge, and Ru K-edge. Extended X-ray absorption fine structure (EXAFS) was collected only at U L_3-edge, Pu L_2-edge, Sr K-edge, Mo K-edge, and Ru K-edge. For uranium, the reference compounds were UO_2, U_4O_9,[28] and U_3O_8,[28] while for plutonium, PuO_2[29] and PuF_3[30] were employed. AmO_2[31] and $U_{0.9}Am_{0.1}O_2$[30] were used as references for Am(IV) and Am(III), respectively. Cerium was fitted using CeO_2 and $CePO_4$, while for Zr, α-ZrO_2 and $Ce_2Zr_2O_7$ experimental spectra were used. Moreover, the calculated β-ZrO_2, γ-ZrO_2, and $SrZrO_3$ XANES spectra were employed. Nd and Y were compared with the experimental spectra of their sesquioxide compounds (Nd_2O_3 and Y_2O_3), and their calculated spectra for a solid solution with UO_2. For Mo, Pd, Rh, and Ru, the reference spectra were collected in their crystallographic structure stable at room temperature: body-centred cubic (BCC) for Mo, hexagonal closed packed (HCP) for Ru, and face-centred cubic (FCC) for Rh and Pd. BaO was used as an experimental reference for barium.

High-Energy Resolution Fluorescence Detection XANES (HERFD-XANES) was performed using a Johann-type X-ray emission spectrometer[38] with Johann-focusing geometry using five spherically bent crystal analyzers with a 1 m bending radius coupled to a fluorescence single recorded by a KETEK silicon drift detector. HERFD-XANES spectra were collected at the maximum of the following emission lines: U $M_{\alpha1}$ (Si220 analyzers), Ce $L_{\alpha1}$ (Ge331 analyzers), Nd $L_{\alpha1}$ (Si331 analyzers), La $L_{\alpha1}$ (Si400 analyzers), and Ba $L_{\alpha1}$ (Ge400 analyzers).

Data treatment was carried out with Athena and Artemis software from the Demeter package[39] and the FDMNES code.[40] When experimental spectra of the compounds of interest were not available, simulated spectra were employed. Calculations were performed using a self-consistent field with the Dirac−Slater approach. The Poisson equation was solved to obtain the Coulomb potential from the superposed self-consistent atomic densities in the considered clusters. The energy-dependent exchange−correlation potential was evaluated using the local density approximation and constructed using the real Hedin−Lundquist formulations. These calculations were based on static atom supercells of at least 30 atoms, and thermally induced disorder was not considered. As recommended by the code manual, for elements with $Z > 36$, a full relativistic approach was used. Since the analyzed materials were polycrystalline, the calculations were performed without ignoring the polarization effect. The broadening of the absorption edge was taken into account by applying a Lorentzian convolution of the full width at half-maximum equal to the core-hole width of the analyzed edge.

3. EXPERIMENTAL RESULTS

3.1. Metallography and Scanning Electron Microscopy

Figure 1 compares the optical microscopy images of SIMMOX compositions S,[25] SM, and SMB. For both the SM and SMB materials, bright white spots corresponding to metallic precipitates are observed, while additional dark gray spots, representative of oxide precipitates, are also visible for the SMB. The samples are made of a matrix (gray background in the figure) and some secondary phases: the so-called white phases (red circles) and gray phases (green arrows).

Table 2 presents the data regarding the geometric density (g/cm^3) and porosity fraction (vol %) of the samples REFMOX,[25] S,[25] SM, and SMB. The geometric density is obtained by a simple ratio of the sample weight and convex volume. The porosity fraction is determined through image processing with an in-house developed Fiji[41] script using a simple grayscale threshold method.

Table 2. Geometric Density (g/cm^3) and Porosity Fraction (vol %) of Samples REFMOX,[25] S,[25] SM, and SMB

	geometric density (g/cm^3)	porosity (vol %)
REFMOX[25]	10.52(7)	2.4(8)
S[25]	10.24(7)	4(1)
SM	9.98(5)	5(2)
SMB	9.78(3)	5.5(9)

It is clear that as more FP surrogates are added, the density decreases, and the porosity increases. As shown in the table, not only does the addition of FP cause a decrease in the density of the material, but both techniques agree that the addition of metallic FP in batch SM has a larger impact than the addition of Ba in batch SMB. This phenomenon can be explained by the characteristic sizes and distributions of the precipitates. The gray phases, induced by the addition of Ba, appear to have a size of at least a few μm in diameter (Figure 1). On the other hand, white phases are present as much tinier sizes (<1 μm) and are known to accumulate at the Grain Boundary (GB).[42,43] The presence of such precipitates at the GB reduces the surface available for actinide diffusion, hindering densification.

Overall, a porosity fraction of <6 vol % is compatible with real irradiated MOX fuel.

In Figure 2, SIMMOX samples are compared to real fast-neutron-irradiated MOX SEM images,[13,42] highlighting the similarities between SIMMOX and irradiated MOX.

3.1.1. White Phases.

Figure 3 presents an SEM-SE (Secondary Electrons) image acquired on one sample of the SMB batch and EDS mapping of Rh, Pd, Ru, and Mo in the same area. Figure 4 shows a larger EPMA mapping of Pu, Mo, Ru, Rh, and Pd.

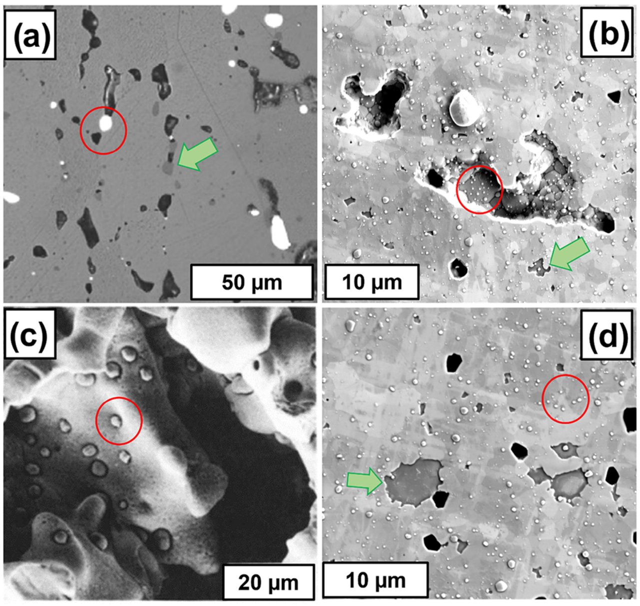

Figure 2. (a, c) SEM micrograph of fast neutron-reactor-irradiated MOX.[13,42] (b, d) SEM micrograph acquired on a sample of batch SMB. The white dots (red circles) represent the white phases, while the darker inclusions (green arrows) are the gray phases. (a) and (c) have been adapted with permission from refs 13 and 42, respectively (Copyright 2020, Elsevier and 1985 Elsevier).

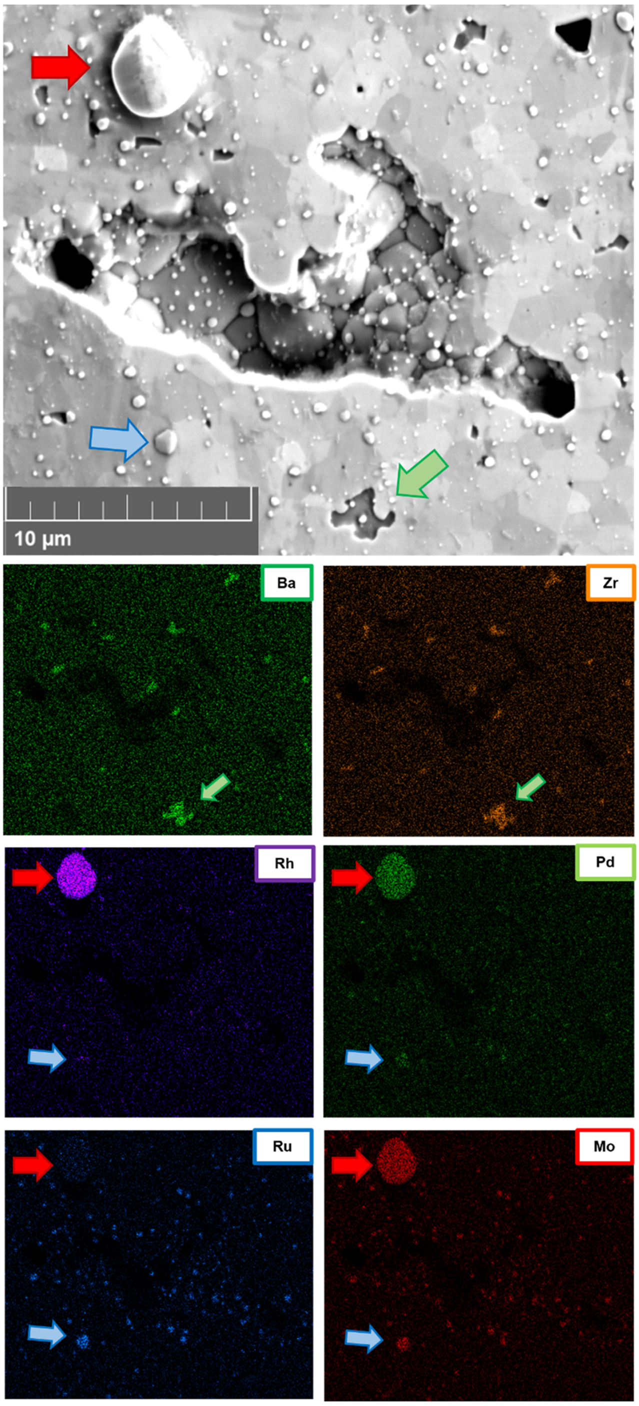

Figure 3. SEM-SE image acquired on one sample of the SMB batch, and EDS mapping of Ba, Zr, Mo, Pd, Rh, and Ru in the same area. The green arrows highlight an example of Ba−Zr inclusion corresponding to the gray phases observed. Red arrows point to an example of "large" (equivalent circle diameter (ECD) > 2 μm) white phase, while blue arrows show a "small" (ECD < 1 μm) white phase.

As shown in Figures 1−4, samples SM and SMB present small white spots, which are representative of the metallic precipitates of the spent nuclear fuel. The sizes of these inclusions vary greatly. Even though the majority of the white phases are nanometric in size, some larger agglomerates are visible, as shown in Figures 3 and 4. These have sizes that can reach up to 30 μm in equivalent circle diameter (ECD) and are homogeneously distributed in the sample volume.

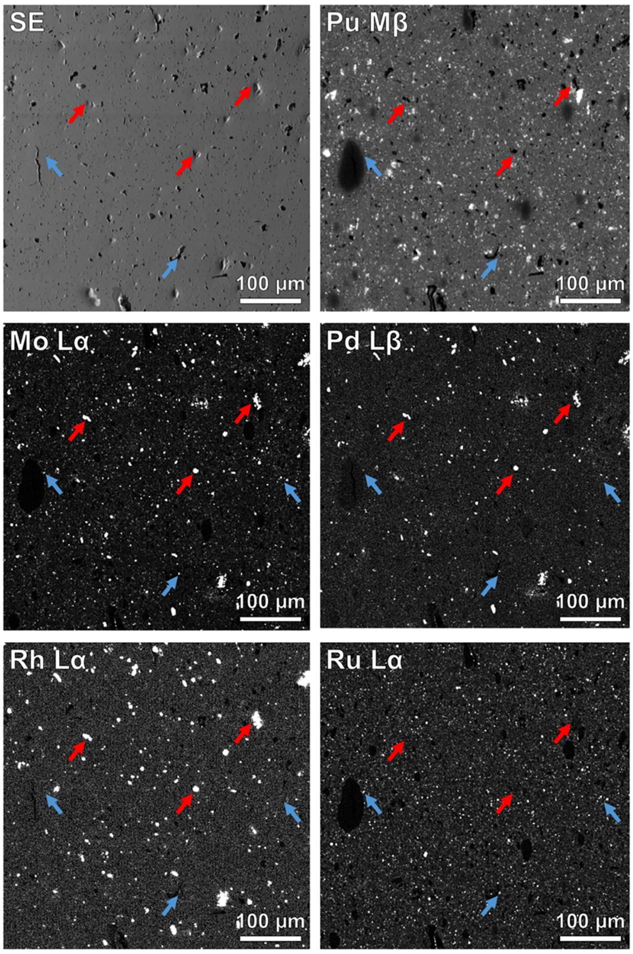

Figure 4. EPMA mapping in SE and in wavelength dispersive X-ray spectroscopy (WDS) at the Pu M_β, Mo L_α, Pd L_β, Rh L_α, and Ru L_α on one sample of the SMB batch (arbitrary grayscale representing the number of counts). The red arrows show the larger Mo−Pd−Rh inclusions, while the blue arrows show the smaller Mo−Ru−Pd inclusions.

Such precipitates are typical of the columnar region of SFR-irradiated MOX,[4,14,42,44] in which the temperature can reach more than 1700 K, thus starting to cause the melting and migration of the Pd-based metallic alloys toward the center of the pellet. This phenomenon is the origin of the largest precipitates, which can reach up to tens of μm in the ECD. This supports the idea that these phases are mainly found as small precipitates (ECD < 1 μm) at the boundaries of $(U,Pu,FP)O_2$ grains, with fewer larger inclusions (ECD > 30 μm) caused by the coalescence and partial melting of the platinoids, which is consistent with the observation on irradiated MOX.[42]

From Figure 3, one can conclude that the FP-based precipitates are mainly sub-μm particles distributed alongside the MOX grain boundaries and at the pore surfaces. These elements were also mapped at a larger scale using EPMA. The results are presented in Figure 4, which shows that the inclusions are distributed all over the pellet. The EDS or WDS maps indicate a strong correlation between the spatial distributions of Mo, Pd, Rh, and Ru, indicating that the majority of these inclusions contain at least three of these elements. Nevertheless, the Ru distribution seems to differ the most from the other three, mainly due to its absence in the largest precipitates, which appear to include Mo−Pd−Rh (highlighted by red arrows in Figures 3 and 4). Inclusions containing Ru (highlighted by blue arrows) appear to also include Mo and Pd, but most do not show traces of Rh (which might be related to the very low amount of Rh included in the sample).

3.1.2. Gray Phases.

Figure 3 shows an example of an SEM-SE image containing multiple gray phase inclusions in sample SMB and the SEM-EDS mapping of the same area. No traces of the BaO and ZrO_2 precursors were found, as observed in previous works on UO_2-SIMfuel.[45] These two compounds have been shown to react, forming $BaZrO_3$, when treated above 1793 K.[43,45] Although these temperatures are usually not reached by PWR fuel during nominal operation, they are commonly observed in fast reactors such as the SFR.

The size of the observed gray phases seems to vary mainly in the range of 1−5 μm, and they are included in the grain structure of the main $(U,Pu,FP)O_2$ matrix. Furthermore, based on the EDS data, the composition of each inclusion can be considered homogeneous, and no "core−shell"-type phase has been found. These core−shell inclusions observed in other works were characterized by three layers: a $(Ba,Sr)(REE,Zr)O_3$ outer shell, an inner core mainly composed of ZrO_2, and an $(U,Zr)O_2$ intermediate layer. Such inclusions are not typical of irradiated UOx or MOX fuel, but they were found in previous work on UO_2-SIMfuel,[45] probably due to an agglomeration phenomenon occurring between the ZrO_2 and $BaCO_3$ precursors during the synthesis process.

In this work, Ba−Zr inclusions will thus be considered as homogeneous Ba−Zr systems. The presence of other elements in smaller quantities (Rare Earth Elements (REE), Sr, Mo) cannot be excluded or confirmed by SEM-EDS analysis alone and will be discussed in the following sections.

3.2. X-ray Diffraction

Figure 5 presents the SP-XRD patterns collected for the three SIMMOX batches. Figure 5 shows the intense reflexes of an FCC phase compatible with the $(U,Pu,FP)O_2$ fluorite matrix, and smaller peaks due to secondary minor phases. The results are presented in Q-space, where $Q = 2\pi \sin(2\theta)/\lambda$, with 2θ being the Bragg angle, and λ the incident X-ray wavelength.

The SP-XRD-derived lattice parameters of the fluorite matrix are 5.444(1), 5.445(1), and 5.446(1) Å for compounds S, SM, and SMB, respectively. These results are between the UO_2 and PuO_2 lattice parameters, 5.470 and 5.396 Å, respectively. Nevertheless, applying Duriez's empirical law[46] $a = 5.47 - 0.074y + 0.32x$ (valid for a MOX $U_{1-y}Pu_yO_{2-x}$) to a stoichiometric ($x = 0$) sample with our composition gives a lattice parameter $a = 5.451$ Å. The discrepancy with the experimental data is likely due to the presence of FP in the solid solution in the $(U,Pu)O_2$ matrix. The other characterization techniques employed in this work are necessary in understanding this lattice parameter shift, and will be discussed together in later sections.

The additional reflexes representing the secondary minor phases have been assigned to the five phases summarized in Table 3: Primitive Cubic (PC) (Space Group (SG) 221: $Pm\bar{3}m$), Face-Centred Cubic (FCC) (SG 225: $Fm\bar{3}m$), Body-Centred Cubic#1 (BCC) (SG 229: $Im\bar{3}m$), BCC#2 (SG 229: $Im\bar{3}m$), and Hexagonal Closed Packed (HCP) (SG 194: $P6_3/mmc$). Both samples, SM and SMB, are characterized by four secondary phases. They share one HCP and two BCC phases, while sample SM presents an FCC phase and SMB a PC phase. The nature of these five observed phases is discussed in the appropriate section of this paper.

3.3. X-ray Absorption Spectroscopy

3.3.1. Metallic FP.

The Rh and Pd K-edge XANES spectra are presented in Figure 6 along with the metallic reference of the respective elements. Metallic Rh and Pd crystallized in the same FCC (SG 225: $Fm\bar{3}m$) structure, in which every atom is 12-coordinated.

The Rh K-edge XANES spectra of sample SMB look almost identical to SM, while palladium shows instead a small but significant difference, appearing flatter in the range of 24,370−24,400 eV. This could be seen as an effect of a more distorted atomic environment, or a shift in speciation.

Both XANES and EXAFS (SI) data analyses confirmed that Ru is completely in the metallic state.

The Mo K-edge XANES spectra of Figure 7 show a clear difference in Mo speciation behavior between samples SM and SMB. In the SM spectrum, two main features (A and B) typical of metallic Mo in different structures are observed.

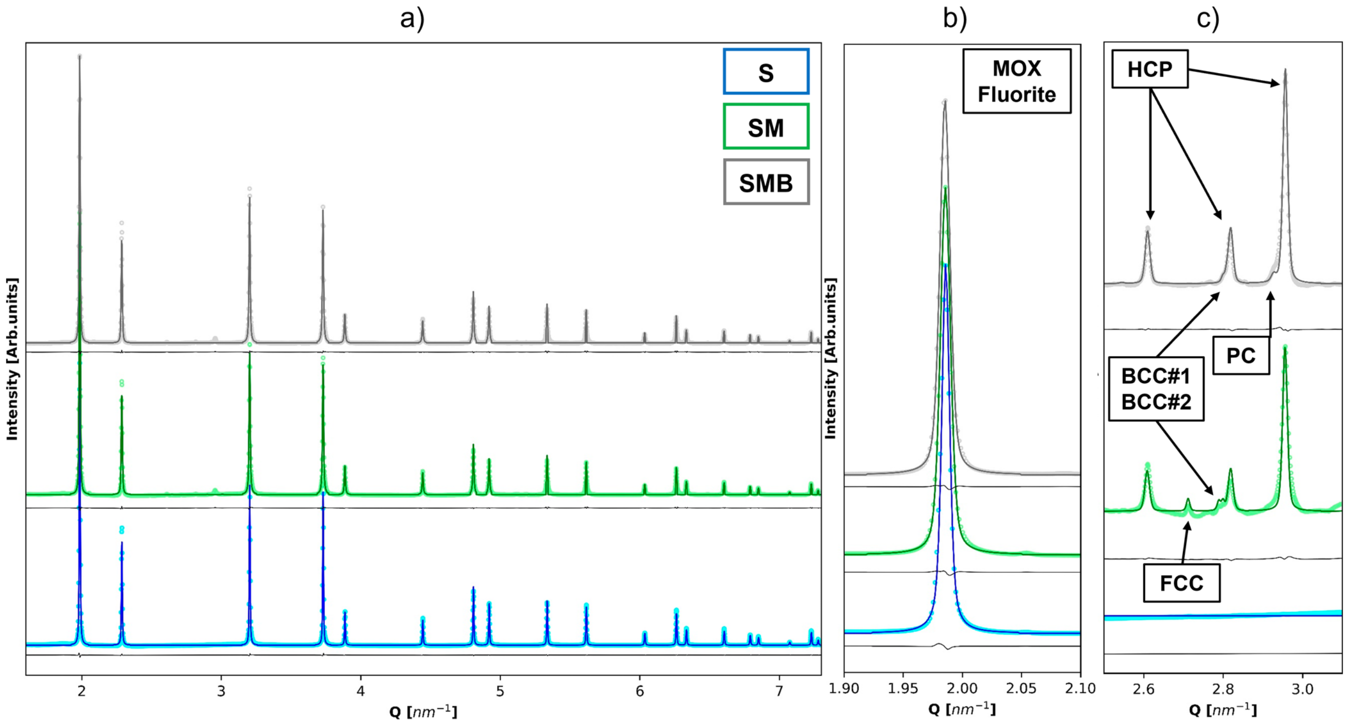

Figure 5. Experimental and fitted SP-XRD patterns collected at 17 keV for the samples S, SM, and SMB: (a) full patterns, (b) magnification of the first fluorite peak, and (c) magnification of the region in which minor phases were identified.

Table 3. Summary of the Identified FP-Based Precipitates and Their Lattice Parameters

	lattice parameter (Å)	
	SM	SMB
fluorite	a = 5.445(1)	a = 5.446(1)
HCP	a = 2.748(1), c = 4.395(1)	a = 2.747(1), c = 4.395(1)
BCC#1	a = 3.130(2)	a = 3.130(2)
BCC#2	a = 3.142(2)	a = 3.120(2)
FCC	a = 3.961(1)	absent
PC	absent	a = 4.228(2)

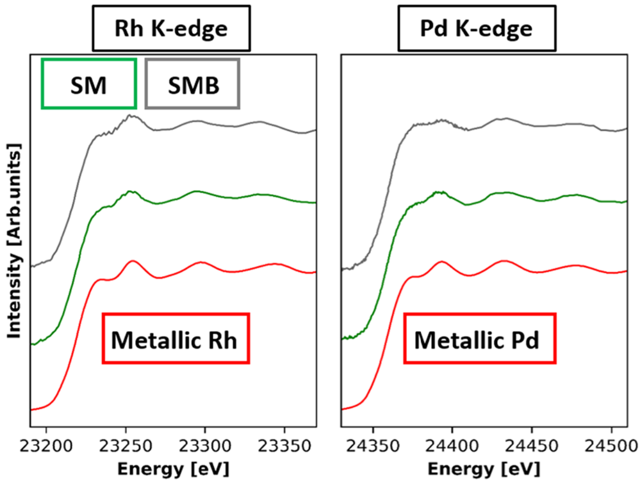

Figure 6. XANES spectra collected at the Rh, Pd, and Ru K-edges for samples SM and SMB.

The XANES signal from sample SM was thus fitted using Linear Combination Fitting (LCF) with the three possible structures for metallic Mo: BCC (SG 229: $Im\bar{3}m$), FCC (SG 225: $Fm\bar{3}m$), and HCP (SG 194: $P6_3/mmc$). To discriminate among the various solutions of the linear combination fittings, we know from both the SP-XRD and Mo–Ru–Pd(Rh) phase diagram[45] that some part of the Mo crystallizes in a BCC (SG 229) structure. Therefore, all the fits that did not include a BCC structure were discarded, knowing that both the SP-XRD and Mo–Ru–Pd(Rh) phase diagram[45] show that some part of the Mo crystallizes in such a lattice. Theoretical calculations cannot differentiate between FCC and HCP structures because of their similar local environments (12 neighbors in the first coordination shell). Mo can be part of all three white phase structures, and there is no reason a priori for Mo not to partake in the formation of FCC or HCP phases. Hence, we have considered that the best description of the speciation of Mo in sample SM is the fitting combination: 31(13)% of FCC, 37(5)% of BCC, and 31(10)% of HCP.

Compared to the SM sample, the white line of the SMB XANES spectrum at the Mo K-edge is shifted toward higher energies, which suggests that molybdenum might be in an oxidized form. Nevertheless, for 19,990 < E (eV) < 20,000, the spectrum still follows the Mo-BCC reference, suggesting that only a fraction of Mo is oxidized, while the rest remains in a metallic state. This agrees with the EXAFS Fourier transforms (FT) collected on sample SMB, exhibiting a new intense feature at ($R + \varphi$) of about 1.4 Å (SI), which is absent in the spectrum of sample SM. Such a peak is typical of an oxygen shell surrounding the absorbing atom. Hence, the linear combination fitting of the XANES signal was performed using all three FCC, HCP, and BCC metallic references as well as both the calculated $BaMoO_3$ and experimental MoO_3 spectra. In $BaMoO_3$ (SG 221), Mo(IV) is surrounded by six equivalent oxygen atoms forming an octahedron. The coordination remains identical in MoO_3, but Mo is hexavalent. From the 26 possible fits, all that did not have any BCC-Mo were discarded. All the eight remaining fits (SI) suggest that in sample SMB, a fraction of Mo is in the metallic state, while the rest is in the +VI oxidation state. The best fit found 55(2)% of Mo in the metallic state (between HCP and BCC), and 45(2)% of Mo oxidized to the 6+ state. MoO_3 is considered insoluble in the UO_2 fluorite structure[47,48] and thus we will assume that Mo with an oxidation state of +VI needs to be found in secondary phases. As no other secondary phases were identified in SP-XRD analysis, we hypothesize

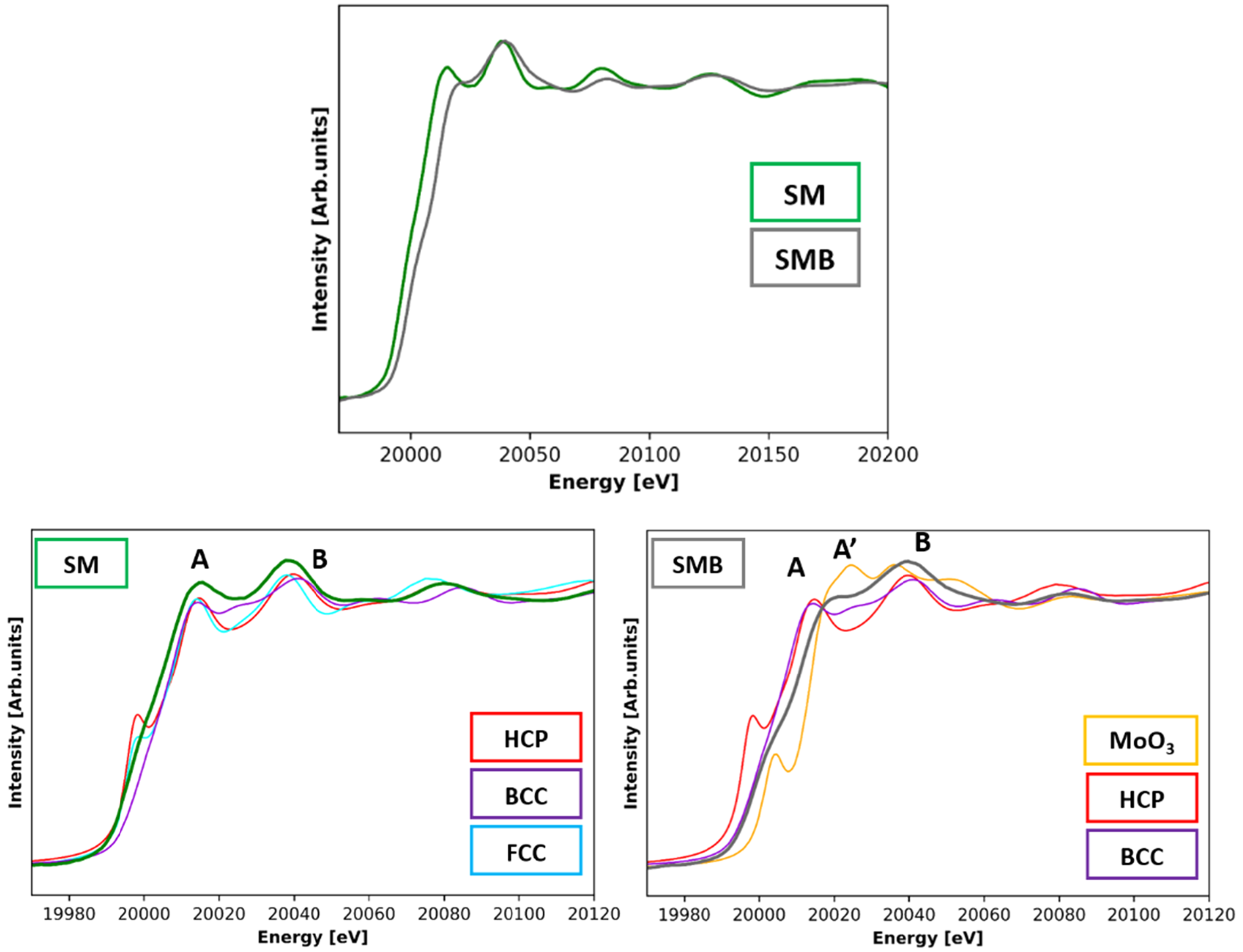

Figure 7. XANES spectra collected at Mo K-edge for samples SM and SMB, along with the most relevant references. Note that FCC and HCP reference spectra were calculated with the FDMNES code. The intense feature at about 20 keV is an artifact due to the erroneous estimation of the Fermi energy at the Mo K-edge.

Table 4. XANES-Derived Oxidation States, and O/An and O/M Ratios

	U	Pu	Am	Ce	La	Nd	Sr	Y	Zr	O/An	O/M
S	4.10(2)	3.89(2)	3.16(2)	3.77(3)	3	3	2	3	4	2.02(2)	1.99(2)
SM	4.18(2)	3.99(2)	3.12(2)	3.71(3)	3	3	2	3	4	2.06(2)	2.03(2)
SMB	4.11(2)	3.91(2)	3.04(5)	3.83(3)	3	3	2	3	4	2.03(2)	2.00(2)

that Mo participated in the formation of gray phases, for example, in cationic substitution on Zr sites in $BaZrO_3$.

3.3.2. Oxidation States and O/M Ratios of Actinides, Rare Earth Elements, Zr, and Ba. Previous works on the U−Pu−Am−O system have shown that mixed oxides, even at stoichiometry (O/M = 2.00), present fractions of nontetravalent cations. Specifically, uranium is found in both 4+ and 5+ oxidation states, and plutonium is found in 3+ and 4+ oxidation states.[49,50] In this work, the actinides L_3-edges XANES data (in SI) show that every sample is composed of a mixture of U(IV), U(V), Pu(III), Pu(IV), Am(III), and Am(IV). This is consistent with the aforementioned literature and with works on doped samples.[25,51] The only sample for which Pu can be considered completely tetravalent is SM, where only 1(2)% of Pu(III) has been observed. In general, the addition of Mo, Pd, Rh, Ru, and Ba induced a slight oxidation of uranium, which passed from an average oxidation state of +4.10(2) for sample S, to +4.18(2) and +4.11(2) for samples SM and SMB. A similar tendency is observed for Pu, while Am is instead characterized by reduction. The average oxidation state for each actinide is presented alongside the FP oxidation states in Table 4. No further analysis of the actinides' behavior will be conducted in this paper, as our main focus is on the secondary FP-based phases formed.

La, Nd, and Ce L_3-edge HERFD-XANES were collected on SM and SMB compounds (Figure 8) and compared with the already published edges of samples S.[25]

La and Nd L_3 spectra overlap perfectly with batch S, for which we concluded that La and Nd local symmetries are consistent with a fluorite solid solution. It is safe to affirm then that also for batch SM and SMB, La and Nd are dissolved into the $(U,Pu,FP)O_2$ matrix, and do not participate significantly in any secondary phase.

Cerium, on the other hand, evolves significantly from one sample to another. The intensity ratio between peaks A and B can be used to qualitatively observe the change in the oxidation state.[52] As presented in Figure 8, batch SM is characterized by a slight Ce reduction (more intense peak A), while in samples SMB, Ce is slightly oxidized (less intense peak A). Performing a quantitative LCF routine gives an

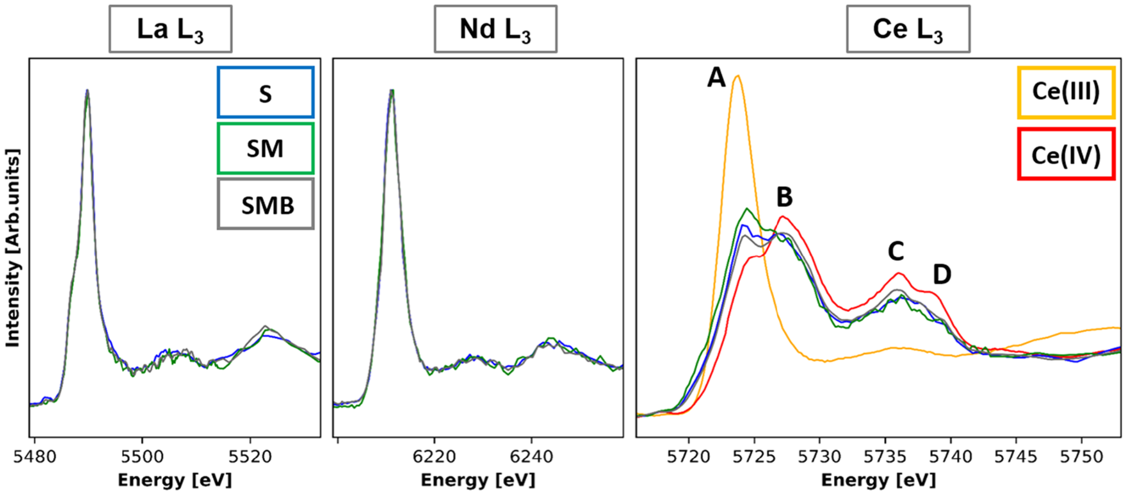

Figure 8. HERFD-XANES collected at the La, Nd, and Ce L$_3$-edges.

average Ce oxidation state of +3.71(3) for batch SM, compared to +3.77(3) for batch S. While for the sample SMB, Ce is found slightly more oxidized, with an oxidation state of +3.83(3).

Ba L$_3$-edge HERFD-XANES is plotted in Figure 9 with BaO (SG 225: $Fm\bar{3}m$) and $BaZrO_3$ (SG 221: $Pm\bar{3}m$) reference spectra. The former has been observed in a previous work on UO_2 SIMfuel,[45] while the latter is representative of the general perovskite-type precipitates making up the gray phases, typical of SFR-irradiated MOX fuel. As expected, we can see that the shape of the white line does not shift among the three spectra, as Ba oxidation state remains 2+ in batch SMB as well as in the references. Significant differences in features (A, B, and C) are, however, observed in the postedge, as both the coordination and Ba−O distances change from BaO to $BaZrO_3$. Overall, the comparison confirms that Ba in the SMB sample is found in a $BaZrO_3$-type structure.

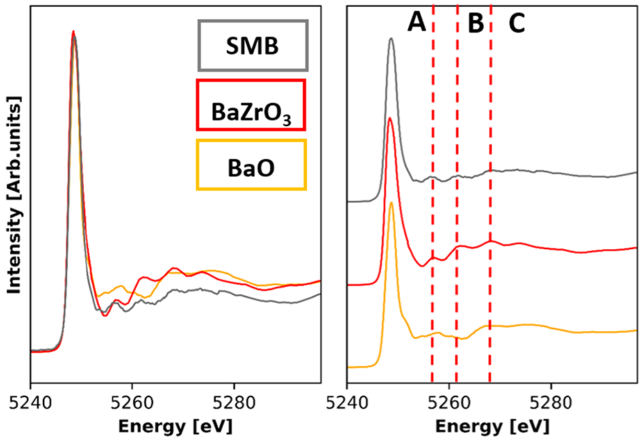

Figure 9. HERFD-XANES at the Ba L$_3$-edges for the L$_{\alpha1}$ transition was collected for the SIMMOX-SMB batch and two references: BaO (orange) and $BaZrO_3$ (red).

As can be seen in the Zr K-XANES spectra in Figure 10, the SM spectrum is similar to that of sample S, in which Zr is completely incorporated into the $(U,Pu,FP)O_2$ solid solution. This behavior agrees with the literature, as the addition of Mo, Ru, Rh, and Pd is not expected to affect Zr speciation. However, a strong change in the white line shape is observed for SMB compared to S and SM. This is consistent with the addition of Ba, as it induces the precipitation of Zr in $BaZrO_3$-type phases. The XANES spectrum of SMB was fitted considering various structural solutions, and it was found that 29(1)% of Zr formed $BaZrO_3$ perovskite-type phases, while the remaining 71(2)% were dissolved within the $(U,Pu,FP)O_2$ solid solution. A partial Zr segregation among these two phases is expected for similar systems.[24,43]

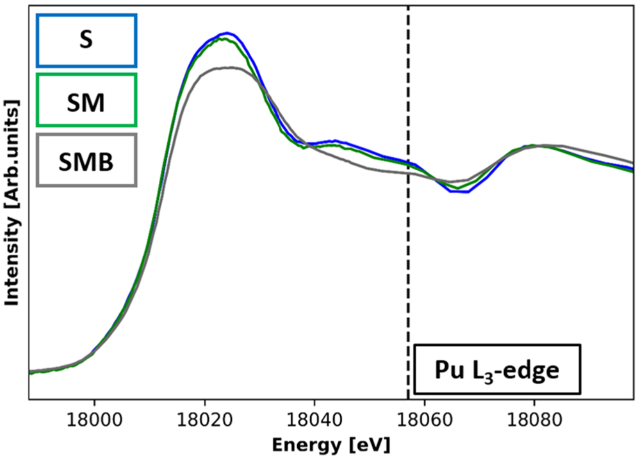

Figure 10. XANES spectra collected at the Zr K-edge.

In Table 4, we can observe that, as expected, since most soluble FP have an oxidation state <4, the O/M is lower than the O/actinides (O/An) value. The O/M ratios are 1.99(2), 2.03(2), and 2.00(2) for S, SM, and SMB, respectively. The difference in O/M between samples S and SMB (1×10^{-2}) is negligible, while sample SM exhibits a slight oxidation (O/M of 2.03(2)). It is worth noting that this oxidation is entirely carried by the actinides.

3.3.3. Local Environment Analysis. U L$_3$ and Pu L$_2$ EXAFS data analysis confirms that all the sample matrices could be considered as almost perfect U−Pu−O fluorite structured, as the quantitative results of the fits and the deduced structural parameters (Figure 11 and SI) are consistent with previous works.[53,54] The structural parameters obtained through the fitting of the EXAFS signal are presented in Table 5. The Pu−O distances are always shorter than the U−O distances, as expected from the respective cationic radii in an 8-coordinated environment: 1.00 and 0.96 Å for U(IV) and Pu(IV), respectively.[55] Looking at the values of the Debye−Waller factor, they are systematically larger for U−O$_1$ than for Pu−O$_1$, for all samples, suggesting that the first oxygen shell is characterized by a greater disorder around uranium atoms. This phenomenon could mean that defects are more concentrated around U sites and thus the local environment is more distorted around uranium atoms than around plutonium atoms.

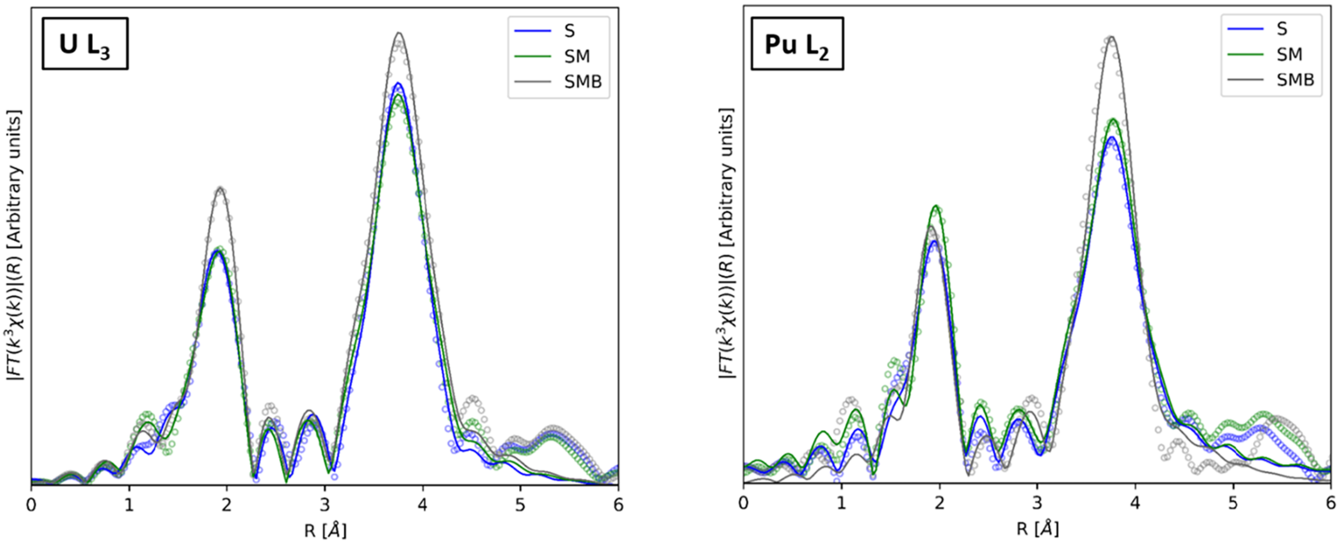

Figure 11. U L_3-edge and Pu L_2-edge EXAFS Fourier Transform (FT) (empty circle markers) and their respective fits (solid line).

Table 5. Structural Parameters[a] Obtained by the Fitting of the EXAFS Signals of Samples from Batches S,[25] SM, and SMB

	SIMMOX-S[25]				SIMMOX-SM				SIMMOX-SMB			
shell	R (Å)	N	N_{th}	σ^2 ($\times10^{-3}$ Å^2)	R (Å)	N	N_{th}	σ^2 ($\times10^{-3}$ Å^2)	R (Å)	N	N_{th}	σ^2 ($\times10^{-3}$ Å^2)
	U-L_3 (R-factor = 0.007)				U-L_3 (R-factor = 0.008)				U-L_3 (R-factor = 0.007)			
U–O_1	2.344(5)	8.0(5)	8	5.6(5)	2.344(5)	8.0(5)	8	5.7(5)	2.351(5)	8.0(5)	8	4.0(5)
U–M	3.852(5)	12.0(5)	12	3.0(5)	3.851(5)	12.0(5)	12	3.0(5)	3.854(5)	12.0(5)	12	1.9(5)
U–O_2	4.50(1)	24.0(5)	24	5(1)	4.50(1)	24.0(5)	24	6(1)	4.50(1)	24.0(5)	24	6(1)
	Pu-L_2 (R-factor = 0.015)				Pu-L_2 (R-factor = 0.009)				Pu-L_2 (R-factor = 0.013)			
Pu–O_1	2.340(5)	8.0(5)	8	3.1(5)	2.338(5)	8.0(5)	8	3.4(5)	2.343(5)	8.0(5)	8	3.3(5)
Pu–M	3.845(5)	12.0(5)	12	1.7(5)	3.845(5)	12.0(5)	12	1.9(5)	3.849(5)	12.0(5)	12	1.6(5)
Pu–O_2	4.47(1)	24.0(5)	24	7(1)	4.45(1)	24.0(5)	24	6(1)	4.44(1)	24.0(5)	24	7(1)

[a] R is the interatomic distance in Å, N is the number of neighboring atoms, which is compared to its theoretical value of a pristine structure N_{th}, and σ^2 is the Debye–Waller factor in Å.

3.4. Electron Probe Microanalysis

The gray phases were further characterized using EPMA, notably through quantitative measurements along the horizontal profiles. The results are shown in Figure 12. Quantitative analysis of white phases' composition is impossible due to their nanometric size, which is much smaller than the electron interaction volume (~1 μm^3). Each data point, therefore, represents an average of tens of small precipitates homogeneously distributed along the material, which makes it impossible to obtain the quantitative composition of individual inclusions. We will focus on the data obtained on the gray phases.

One can observe that both Ba and Zr profiles present spikes that correspond to the Ba–Zr precipitates observed in Figure 3. For Zr, the average content in the matrix is close to 0.6 wt %, which is lower than the amount added to the sample and that observed in Sample S, in which the content in the matrix was close to that of the sample.[25] A significant part of Zr thus appears to be included in the Ba–Zr inclusions. Considering Ba, its content outside of the Ba–Zr inclusions is low (mostly below 0.3 wt %), but only falls below its detection limit (generally around 0.06 wt %) in the U-rich areas observed in the 120–145 μm zone of the profile. This could correspond to contributions from submicronic Ba–Zr inclusions, such as those observed in Figure 3, and/or a small amount of Ba diluted in the matrix.

Additionally, the Ce concentration spikes in the regions corresponding to the gray phases, as shown in Figure 12a. This is consistent with the registered solubility of REE in such structures, which are generally referred to as $(Ba,Sr)(Zr,REE,Mo)O_3$. Nevertheless, neither systematic nor significant enrichment is observed in this area for La, Nd, and Y. This suggests that trivalent REE might partake in the formation of such precipitates, but not in large quantities, leaving Ce and Mo as the prevalent cations substituting Zr(IV).

Sr is observed in solution in the $(U,Pu,FP)O_2$ matrix, but significant concentration spikes appear inside the Ba–Zr precipitates, which is expected since Sr is well-known to substitute in the Ba sites. We also observe significant Sr enrichment inside the U-rich zones, as previously observed in the S sample.[25] This enrichment remains low (below 0.2 wt %), but is significantly higher than in the matrix (in which it is mostly below 0.1 wt %), considering both the standard deviation and the detection limit.

As shown in Figures 4 and 12, the U and Pu homogeneity in samples SM and SMB is comparable to that of sample S, even with the additional FP precursors employed.

4. DISCUSSION

4.1. MOX Matrix $(U,Pu,Am,FP)O_2$

From the SP-XRD and EXAFS data, we can deduce that the crystallographic structure of $(U,Pu,FP)O_2$ is fluorite-like (SG 225: $Fm\bar{3}m$), with structural parameters described in Table 5.

The difference in the lattice parameters between S (5.444(1) Å) and SM (5.445(1) Å) is negligible, while that between S and SMB (5.446(1) Å) is large enough to be discussed. The first hypothesis to explain this tendency is the different O/M ratios in the $(U,Pu,FP)O_2$ solid solutions; in particular, it is known that reducing the actinides causes lattice swelling. This effect is described by the Duriez law,[46] which reads

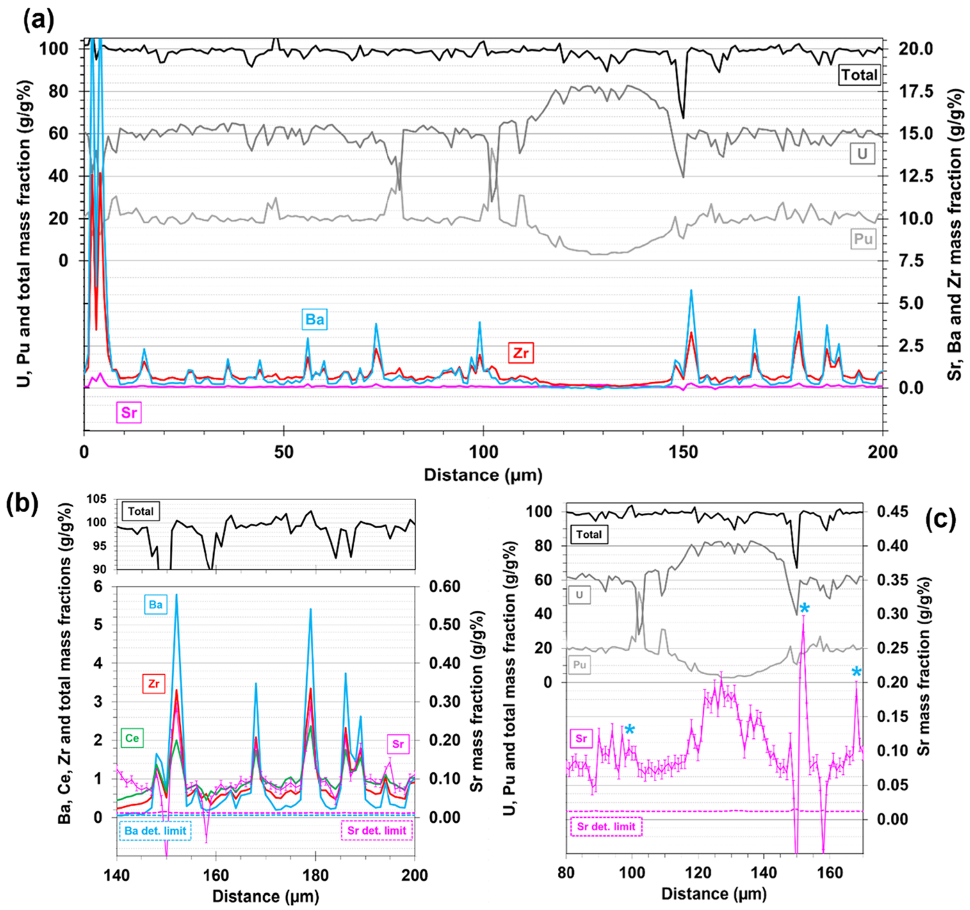

Figure 12. Quantitative EPMA profile over a distance of 200 μm. Mass fractions for U (dark gray), Pu (light gray), and the total (black) are indicated on the left y-axis, while those of Ba (cyan), Sr (pink), and Zr (red) are indicated on the right y-axis. (a) Close-up of Ba-based inclusions. (b) Close-up of U-enriched area. Ba-based precipitates are indicated by blue stars. In (a) and (b), the detection limits for Ba and Sr along the line are also given (those of Zr and Ce were below that of Ba). (c) Magnification of the region 80−170 μm of subfigure (a), rescaled to highlight Sr distribution. The error bar for Sr corresponds to the expected statistical dispersion ($k = 3$) based on the number of counts measured at the peak and the background of the sample and reference materials.

$$a\ (\text{Å}) = 5.47 - 0.074y + 0.32x$$

where a is the lattice parameter of the $U_{1-y}Pu_yO_{2-x}$ solid solution, y is the plutonium incorporation rate, and x is the departure from the ideal stoichiometry in oxygen. Even though this relationship does not take into account the FP effect on the structure, we can use it to loosely estimate the effect of O/M on the lattice parameter. The reduction from O/M = 2.00 to O/M = 1.99, as determined from XANES, should induce a lattice parameter increase of 3.2×10^{-3} Å, which is much larger than the difference observed herein.

This observation is particularly important in the context of this work since the effects observed by the various experimental techniques used are generally very small with respect to their associated uncertainties and can sometimes appear at the limits of the associated margins of error. In the present case, the O/M ratio determined by HERFD-XANES differs only by 0.01, which is within the uncertainty. This technique alone cannot, therefore, be used to conclude the real effect of the incorporation of nonsoluble FPs on O/M. The complementary use of another analytical method, in this case SP-XRD, is therefore essential to highlight such an impact, which, even if minimal, remains very real.

The slight swelling of the lattice could also be explained by the interaction of the added FP (Ba, Mo, Pd, Rh, Ru) with the soluble FP. For example, Sr, Zr, and Ce are known to precipitate into perovskite-type phases due to their interaction with Ba.[42,44] This phenomenon would induce the partitioning of soluble FP between the matrix solid solution and precipitates, causing lattice expansion. From the data collected in other works,[56−58] for example, only the complete precipitation of Sr and Zr in secondary phases would cause a swelling in the solid solution of about 1.3×10^{-3} Å, which would also be consistent with the small but significant increase in the lattice parameter observed experimentally. XAS analysis of the Zr K-edge has confirmed that 29(1)% Zr precipitated in perovskite-type structures, while 71(1)% still remained in the solid solution inside the $(U,Pu,Am,FP)O_2$ matrix.

The matrices of samples SM and SMB also completely incorporate La and Nd, whose HERFD-XANES spectra (Figure 8) are similar to those collected for sample S. This confirms that the speciation of these two elements is not significantly affected by the presence of Mo, Pd, Rh, Ru, and Ba.

The behaviors of Ce, Sr, and Zr are unchanged from S to SM, as expected, since the introduction of platinoids and Mo does not affect their speciation. On the other hand, the EPMA data (Figure 12) show evidence of the precipitation of Ce, Sr, and Zr in sample SMB. In particular, Ce segregation could cause a shift in the O/M ratio depending on its oxidation state. If we consider the extreme possibility that all the Ce included in the gray phases had to be 4+, as it theoretically should be in order to substitute on the Zr sites, and that all the cerium left in the (U,Pu,Am,FP)O_2 solid solution is 3+, the O/M would be reduced by roughly 6×10^{-4} and thus negligible compared to the experimental uncertainty (2×10^{-2}). Therefore, the participation of Ce in the gray phases cannot account for the slight variation in O/M between sample SM (O/M = 2.03(2)) and sample SMB (O/M = 2.00(2)). The precipitation of Sr would, on the other hand, increase the O/M ratio by about 4×10^{-5}, an even smaller value. The formation of gray phases does not therefore directly affect the O/M ratio of the matrix in a measurable way, and is still smaller than the difference experimentally measured of 0.03(2).

4.2. FP Precipitates and Phase Identification

4.2.1. Gray Phases. Looking at the SP-XRD patterns, the reflexes present only in SMB can be assigned to a perovskite-type structure, as only Ba contributes to the formation of gray phases. Indeed, these reflexes have been indexed as a primitive cubic structure (SG 221: $Pm\overline{3}m$) with a lattice parameter of 4.228(2) Å. The HERFD-XANES of the Ba L_3-edge (Figure 9) points toward a 12-coordinated environment, like a $BaZrO_3$-type structure. The XANES of the Zr K-edge (Figure 10) is also consistent with such a compound. SEM-EDS (Figure 3), and EPMA profiles (Figure 12) reveal Ba-Zr-based inclusions characterized by an enrichment in Ce and Sr with respect to the (U,Pu,Am,FP)O_2 matrix. All characterization techniques employed are consistent in identifying the gray phases as (Ba,Sr)(Zr,Ce,Mo)O_3-type inclusions.

The lattice parameter of a pure $BaZrO_3$ perovskite, crystallizing in a primitive cubic structure (SG 221: $Pm\overline{3}m$), is given in the literature as 4.190 Å.[59] The discrepancy between the theoretical lattice parameter and the measured one (4.228(2) Å) can be understood from cationic substitutions. A recent work on similar phases has indeed shown that the substitution of Sr on the Ba site, and of Ce on the Zr site, could lead to a lattice parameter of 4.219(2) Å.[24]

4.2.2. White Phases. In order to correctly identify the remaining reflexes, we used the phase diagram at 1000 and 1700 K of the ternary system Mo−Ru−Pd (SI). Rh and Pd in their pure metallic states crystallize in the same FCC (SG 225: $Fm\overline{3}m$) structure, and have similar atomic radii of 1.342 and 1.373 Å, respectively.[60] For the sake of simplicity, Rh is therefore often omitted in the phase diagram, and its content is added to Pd using the notation Pd(Rh).

According to the literature, the observed precipitates in irradiated fuel studies are of three kinds: α-phase (FCC—SG 225—$Fm\overline{3}m$), β-phase (BCC—SG 229—$Im\overline{3}m$), and ε-phase (HCP—SG 194—$P6_3/mmc$).[42−44] In the ternary phase diagram Mo−Ru−Pd(Rh) (in SI), these structures correspond to alloys enriched in Pd(Rh), Mo, and Ru, respectively. These crystallographic structures were hence used to fit the SP-XRD patterns.

In sample SM, we identified four phases, namely two BCC (called BCC#1 and BCC#2), one FCC, and one HCP. For batch SMB instead, only three phases were observed: two BCC and one HCP.

According to the phase diagram (in SI), the HCP phase should be the most abundant, which, at first approximation, is consistent with the intensity of their reflexes. From the phase diagram, the presence of an FCC phase can also be expected, even in smaller quantities compared to the HCP one. Reflexes corresponding to this structure are observed for batch SM but not for batch SMB, which could suggest a shift in the speciation of the Mo−Ru−Pd(Rh) system due to the addition of Ba in the system.

Among the four elements forming the metallic precipitates, Pd has the lowest melting point (1828 K) compared to the 2236, 2607, and 2896 K of Rh, Ru, and Mo, respectively.[61,62] Furthermore, Pd is the only element whose melting temperature is below the sintering plateau temperature (1973 K). Part of the Pd inventory will then inevitably melt, probably causing the migration and partial segregation of Pd-rich alloys. This phenomenon can explain the presence of FCC phases in the material, as these Pd-rich alloys crystallize during cooling after the sintering plateau. Moreover, the remaining Pd-depleted alloys would easily create agglomerates with BCC structures, as at 1000 K, the Mo−Ru alloys are characterized by a large biphasic HCP-BCC domain. This hypothesis is well supported by the SEM-EDS and EPMA mapping data (Figures 3 and 4), which also highlight a correlation between the size and composition of the metallic precipitates. The "larger" particles (ECD > 1 μm) (red arrows in Figures 3 and 4) are made of mainly Pd−Rh−Mo, the Ru-containing inclusion (which shows the presence of Ru and Mo) is mostly made of "smaller" particles (ECD < 1 μm, blue arrows in Figures 3 and 4).

The BCC (β) phases are very similar and are characterized by lattice parameters (3.130(2) and 3.142(2) Å) that are very close to those of pure Mo (3.14 Å). The shrinking of the interatomic distances in the structure is expected since Mo has the largest metallic radius among the four discussed elements: 1.386 Å (Mo), 1.373 Å (Pd), 1.342 Å (Rh), and 1.336 Å (Ru).[60] It is then expected that Mo-rich alloys of these elements would present a slightly smaller lattice parameter than pure Mo. The evolution of the lattice parameters of the BCC#1 and BCC#2 phases observed between the samples SM and SMB must be related to the difference in Mo speciation highlighted by the XAS analysis. Since part of the Mo inventory is oxidized in sample SMB (while 100% is metallic in sample SM), the overall composition of the white phases is inevitably altered, thus leading to varying crystallographic parameters.

Oxidized Mo is likely to participate in the formation of gray phases since no other secondary phases are observed by SP-XRD. Another possibility we investigated was the precipitation of the nanometric particles of MoO_3 at the grain boundaries. Nevertheless, there is no reason for this process to occur in sample SMB and not in sample SM. The Mo concentration, synthesis route, and parameters are the same for batches SM and SMB, with the only difference being the addition of Ba in sample SMB. The shift in Mo speciation is likely due to the presence of Ba and thus the inclusion of Mo in the formation of gray phases.

The measured lattice parameter of the FCC phases (α) is slightly larger than that of pure Pd. Our hypothesis is that an alloy with elements characterized by a larger atomic radius, such as Mo, would cause swelling of the lattice parameters of the FCC structure.

The last phase identified as the metallic inclusion is the HCP phase corresponding to the Ru-rich alloys. The lattice parameters of a theoretically perfectly packed HCP structure, a and c, are related by the ratio $c/a = 2\sqrt{(2/3)} \approx 1.63$. Nevertheless, pure HCP Ru has been observed to be

Table 6. Summary of Identified FP-Based Precipitates[a]

		lattice parameter (Å)			
		SM	SMB	phase identification	reference compound
white phase	HCP: $P6_3/mmc$	a = 2.748(1) c = 4.395(1)	a = 2.747(1) c = 4.395(1)	Ru-based alloy (ε-phases)	HCP Ru a = 2.707 Å c = 4.279 Å
	BCC#1: $Im\bar{3}m$	a = 3.130(2)	a = 3.130(2)	Mo-based alloys (β-phases)	BCC-Mo
	BCC#2: $Im\bar{3}m$	a = 3.142(2)	a = 3.120(2)		a = 3.146 Å
	FCC: $Fm\bar{3}m$	a = 3.961(1)	absent	Ru−Pd−Rh alloy depleted in Mo (α-phases)	FCC Pd a = 3.890 Å
gray phase	PC: $Pm\bar{3}m$	absent	a = 4.228(2)	perovskite	primitive cubic $BaZrO_3$ a = 4.190 Å

[a] The data from the lattice parameters of the reference compounds (last column on the right) are taken from refs 59,63−646566.

characterized by c/a = 1.582, increasing with the addition of Mo in the alloy up to c/a = 1.626.[63] Computing such a ratio with the data found in Table 3 leads to c/a = 1.599(1), which is consistent with the established range of 1.582−1.626 Å. This strongly suggests that this HCP phase may be a Ru-rich alloy with a large Mo presence, which is consistent with the EPMA mapping data presented in Figure 4.

XANES and EXAFS data (Figures 6, 7, and SI) collected at the Mo, Pd, Rh, and Ru K-edges strongly support this hypothesis for sample SM. In this specimen, Rh and Pd K-edge XANES spectra (Figure 6) are remarkably similar to those of the corresponding metallic references. This supports the idea that Rh- and Pd-rich alloys make up the FCC phases identified in sample SM. Both XANES (Figure 6) and EXAFS (in SI) data analyses confirmed that Ru is in a metallic state with an HCP structure (SG 194: $P6_3/mmc$), which can only be attributed to Ru-rich alloys.

Table 6 summarizes the secondary phases identified in samples SM and SMB. Batch S is not present in the table as no secondary phases are observed.

5. CONCLUSION

This work focused on the further development of the SIMMOX approach for the study of irradiated MOX chemistry. Two new sample batches have been produced with the same synthesis/fabrication route proposed in our previous work,[25] in order to study the FP-based secondary phases of irradiated MOX. The microstructures of these samples are representative of real irradiated MOX, exhibiting the same families of secondary phases. By leveraging our separation-of-effects study alongside a multiscale analytical approach, we gained novel insights into the FP interactions.

We examined the speciation of the metallic white phases and uncovered new details regarding the partial segregation of their constituents (Mo, Pd, Rh, Ru) and their correlation with the distinct crystallographic phases observed. Additionally, we investigated the effect of barium (Ba) on the speciation of other fission products. Our findings reveal that the chemical behavior of several fission products shifts with the addition of Ba. Notably, Zr precipitates into Ba-rich phases identified as $BaZrO_3$ perovskite, and Ba also induces the oxidation of Mo, thereby altering the speciation of the metallic precipitates.

This worked proved that the SIMMOX approach can indeed help answer crucial questions in nuclear fuel science. The next step will involve applying the SIMMOX methodology to simulate accidental scenarios involving irradiated nuclear fuel, further enhancing our understanding of these complex systems.

■ ASSOCIATED CONTENT

Data Availability Statement

The relevant data supporting this article have been included as part of the Supporting Information. The Demeter suite has been employed for XAS data treatment, and can be found at https://bruceravel.github.io/demeter/ with 10.1107/S0909049505012719.

Supporting Information

The Supporting Information is available free of charge at https://pubs.acs.org/doi/10.1021/acs.inorgchem.5c04163.

Additional XANES and EXAFS spectra of Ru, Rh, Pd, and Mo; quantitative results of the fitting routines; ternary phase diagram of Mo−Ru−Pd(Rh) at 1973 K (PDF)

■ AUTHOR INFORMATION

Corresponding Author

Philippe Martin − *CEA, DES, ISEC, DMRC, Univ Montpellier, 30200 Marcoule, France;* orcid.org/0000-0003-2743-2068; Email: philippe-m.martin@cea.fr

Authors

Rafael Caprani − *CEA, DES, ISEC, DMRC, Univ Montpellier, 30200 Marcoule, France;* orcid.org/0009-0009-8196-3661

Damien Prieur − *The Rossendorf Beamline at ESRF, The European Synchrotron, 38043 Grenoble, France; Institute of Resource Ecology, Helmholtz Zentrum Dresden Rossendorf, Dresden 01328, Germany*

Julien Martinez − *CEA, DES, ISEC, DMRC, Univ Montpellier, 30200 Marcoule, France*

Florent Lebreton − *CEA, DES, ISEC, DMRC, Univ Montpellier, 30200 Marcoule, France;* orcid.org/0000-0003-4714-8021

Elena F. Bazarkina − *The Rossendorf Beamline at ESRF, The European Synchrotron, 38043 Grenoble, France; Institute of Resource Ecology, Helmholtz Zentrum Dresden Rossendorf, Dresden 01328, Germany*

Kristina O. Kvashnina − *The Rossendorf Beamline at ESRF, The European Synchrotron, 38043 Grenoble, France; Institute of Resource Ecology, Helmholtz Zentrum Dresden Rossendorf, Dresden 01328, Germany;* orcid.org/0000-0003-4447-4542

Denis Menut − *Departementale 128, Synchrotron SOLEIL, L'Orme des Merisiers, 91190 Gif-sur-Yvette, France;* orcid.org/0000-0001-8657-3333

Méghan Alibert − *CEA, DES, ISEC, DMRC, Univ Montpellier, 30200 Marcoule, France*
Stéphanie Lecoq − *CEA, DES, ISEC, DMRC, Univ Montpellier, 30200 Marcoule, France*
Nicolas Clavier − *Institut de Chimie Séparative de Marcoule, Univ Montpellier, CEA, CNRS, ENSCM, 30200 Marcoule, France*

Complete contact information is available at: https://pubs.acs.org/10.1021/acs.inorgchem.5c04163

Author Contributions

R.C.: data curation, conceptualization, formal analysis, investigation, methodology, software, validation, writing—original draft, writing—review and editing, visualization. P.M.: conceptualization, data curation, formal analysis, investigation, methodology, supervision, writing—review and editing, funding acquisition, resources. D.P.: conceptualization, data curation, formal analysis, investigation, supervision, funding acquisition, writing—review and editing. J.M.: conceptualization, investigation, supervision, writing—review and editing, funding acquisition, resources. F.L.: data curation, formal analysis, investigation, methodology, software, validation, writing—review and editing, visualization, resources. E.F.B.: data curation, formal analysis, investigation, methodology. K.O.K.: data curation, formal analysis, investigation, software, validation, writing—review and editing, methodology. D.M.: conceptualization, data curation, formal analysis, investigation, software, validation, writing—review and editing, methodology. M.A.: investigation. S.L.: investigation. N.C.: conceptualization, project administration, supervision, writing—review and editing, resources.

Notes

The authors declare no competing financial interest.

■ ACKNOWLEDGMENTS

This work was supported by the Cross-Cutting Basic Research Program (RTA Program) of the CEA Energy Division and by the Institute of Resource Ecology (IRE) of HZDR. We acknowledge SOLEIL and ESRF for the provision of synchrotron radiation facilities.

■ REFERENCES

(1) Bairiot, H.; Deramaix, P. MOX Fuel Development: Yesterday, Today and Tomorrow. *J. Nucl. Mater.* **1992**, *188*, 10−18.

(2) Bagheri, N.; Nosratinia, F.; Zahakifar, F.; Yousefi, T. The Effect of Operational Parameters on the Properties of Thorium Uranium Oxide Produced via Oxalates' Coprecipitation. *Sci. Rep.* **2025**, *15* (1), No. 18536.

(3) Lebreton, F.; Belin, R. C.; Prieur, D.; Delahaye, T.; Blanchart, P. In Situ Study of the Solid-State Formation of U1−XAmxO2±δ Solid Solution. *Inorg. Chem.* **2012**, *51* (17), 9369−9375.

(4) Guerin, Y. Fuel Performance of Fast Spectrum Oxide Fuel. In *Comprehensive Nuclear Materials*; Konings, R. J. M., Ed.; Elsevier: Oxford, 2012; Chapter 2.21, pp 547−578.

(5) Locatelli, G.; Mancini, M.; Todeschini, N. Generation IV Nuclear Reactors: Current Status and Future Prospects. *Energy Policy* **2013**, *61*, 1503−1520.

(6) Milena-Pérez, A.; Rodríguez-Villagra, N.; Feria, F.; Aguado, C.; Herranz, L. E. Critical Review of Fuel Oxidation Database under Dry Storage Conditions. *Prog. Nucl. Energy* **2023**, *165*, No. 104914.

(7) Milena-Pérez, A.; Bonales, L. J.; Rodríguez-Villagra, N.; Galán, H. Exploring the Impact of Temperature and Oxygen Partial Pressure on the Spent Nuclear Fuel Oxidation during Its Dry Management. *Sci. Rep.* **2023**, *13* (1), No. 1966.

(8) Veliscek-Carolan, J. Separation of Actinides from Spent Nuclear Fuel: A Review. *J. Hazard. Mater.* **2016**, *318*, 266−281.

(9) Sureda, R.; Martínez-Lladó, X.; Rovira, M.; de Pablo, J.; Casas, I.; Giménez, J. Sorption of Strontium on Uranyl Peroxide: Implications for a High-Level Nuclear Waste Repository. *J. Hazard. Mater.* **2010**, *181* (1), 881−885.

(10) Stitt, C. A.; Hart, M.; Harker, N. J.; Hallam, K. R.; MacFarlane, J.; Banos, A.; Paraskevoulakos, C.; Butcher, E.; Padovani, C.; Scott, T. B. Nuclear Waste Viewed in a New Light; a Synchrotron Study of Uranium Encapsulated in Grout. *J. Hazard. Mater.* **2015**, *285*, 221−227.

(11) McMaster, S. A.; Ram, R.; Faris, N.; Pownceby, M. I. Radionuclide Disposal Using the Pyrochlore Supergroup of Minerals as a Host Matrix—A Review. *J. Hazard. Mater.* **2018**, *360*, 257−269.

(12) Mao, K. S.; Gerczak, T. J.; Harp, J. M.; McKinney, C. S.; Lach, T. G.; Karakoc, O.; Nelson, A. T.; Terrani, K. A.; Parish, C. M.; Edmondson, P. D. Identifying Chemically Similar Multiphase Nanoprecipitates in Compositionally Complex Non-Equilibrium Oxides via Machine Learning. *Commun. Mater.* **2022**, *3* (1), No. 21.

(13) Cappia, F.; Tanaka, K.; Kato, M.; McClellan, K.; Harp, J. Post-Irradiation Examinations of Annular Mixed Oxide Fuels with Average Burnup 4 and 5% FIMA. *J. Nucl. Mater.* **2020**, *533*, No. 152076.

(14) Le Gall, C.; Reboul, S.; Fayette, L.; Blay, T.; Zacharie-Aubrun, I.; Félines, I.; Hanifi, K.; Roure, I.; Bienvenu, P.; Audubert, F.; Pontillon, Y.; Hazemann, J.-L. Fission Product Speciation in the VERDON-3 and VERDON-4 MOX Fuels Samples. *J. Nucl. Mater.* **2020**, *530*, No. 151948.

(15) Le Gall, C.; Reboul, S.; Fayette, L.; Blay, T.; Zacharie-Aubrun, I.; Félines, I.; Hanifi, K.; Roure, I.; Bienvenu, P.; Audubert, F.; Pontillon, Y.; Hazemann, J.-L. MOX Fuel Microstructural Evolution during the VERDON-3 and 4 Tests. *J. Nucl. Mater.* **2020**, *531*, No. 152015.

(16) Maeda, K.; Sasaki, S.; Kato, M.; Kihara, Y. Radial Redistribution of Actinides in Irradiated FR-MOX Fuels. *J. Nucl. Mater.* **2009**, *389* (1), 78−84.

(17) McKinney, C.; Hilty, F.; Murray, D.; Poudel, N.; Cappia, F.; Pavlov, T.; Aitkaliyeva, A. Three-Dimensional Microstructural Characterization of FBR MOX Fuel and the Contribution of Microstructural Features to the Thermal Conductivity of the Fuel. *J. Nucl. Mater.* **2022**, *572*, No. 154073.

(18) Parrish, R. J.; Wright, K. E.; Winston, A. J.; McKinney, C.; Harp, J. M.; Aitkaliyeva, A. Characterization of Solid Fission Products in 13.7% FIMA MOX Fuel Using Electron Microscopy Techniques. *J. Nucl. Mater.* **2019**, *524*, 67−79.

(19) Lucuta, P. G.; Verrall, R. A.; Matzke, H.; Palmer, B. J. Microstructural Features of SIMFUEL — Simulated High-Burnup UO_2-Based Nuclear Fuel. *J. Nucl. Mater.* **1991**, *178* (1), 48−60.

(20) Lucuta, P. G.; Matzke, H.; Verrall, R. A. Thermal Conductivity of Hyperstoichiometric SIMFUEL. *J. Nucl. Mater.* **1995**, *223* (1), 51−60.

(21) Matzke, H.; Lucuta, P. G.; Verrall, R. A.; Henderson, J. Specific Heat of UO_2-Based SIMFUEL. *J. Nucl. Mater.* **1997**, *247* (Suppl C), 121−126.

(22) Matzke, H.; Lucuta, P. G.; Verrall, R. A. Formation and Behaviour of Barium Silicate in UO_2-Based SIMFUEL. *J. Nucl. Mater.* **1991**, *185* (3), 292−296.

(23) Santos, B. G.; Nesbitt, H. W.; Noël, J. J.; Shoesmith, D. W. X-Ray Photoelectron Spectroscopy Study of Anodically Oxidized SIMFUEL Surfaces. *Electrochim. Acta* **2004**, *49* (11), 1863−1873.

(24) Geiger, E.; Guéneau, C.; Alpettaz, T.; Bonnet, C.; Chatain, S.; Tougait, O.; Menut, D.; Bellayer, S.; Hunault, M. O. J. Y.; Corcoran, E. C. Fission Products Chemistry in Simulated PWR Fuel up to 2100°C: Experimental Characterisation and TAF-ID Modelling. *J. Nucl. Mater.* **2022**, *572*, No. 154040.

(25) Caprani, R.; Martin, P.; Prieur, D.; Martinez, J.; Hunault, M. O. J. Y.; Lebreton, F.; Desagulier, M.-M.; Aloin, C.; Picard, L.; Alibert, M.; Gabriel, G.; Signoret, P.; Clavier, N. Fission Products Speciation

in Nuclear Fuel: Synthesis and Characterisation of Mixed Oxide (U,Pu)O2 SIMfuel. *J. Nucl. Mater.* **2023**, *585*, No. 154607.

(26) Merlet, C. An Accurate Computer Correction Program for Quantitative Electron Probe Microanalysis. *Microchim. Acta* **1994**, *114–115* (1), 363–376.

(27) Ancey, M.; Bastenaire, F.; Tixier, R. *Microanalysis and Scanning Electron Microscopy*; Orsay: Éditions de Physique, 1980.

(28) Sitaud, B.; Solari, P. L.; Schlutig, S.; Llorens, I.; Hermange, H. Characterization of Radioactive Materials Using the MARS Beamline at the Synchrotron SOLEIL. *J. Nucl. Mater.* **2012**, *425* (1), 238–243.

(29) Kieffer, J.; Valls, V.; Blanc, N.; Hennig, C. New Tools for Calibrating Diffraction Setups. *J. Synchrotron Radiat.* **2020**, *27* (2), 558–566.

(30) Rodriguez-Carvajal, J. In *Introduction to the Program FULLPROF: Refinement of Crystal and Magnetic Structures from Powder and Single Crystal Data*, Commission for Powder Diffraction, IUCr, Newsletter, 2001; Vol. 26, pp 12–19.

(31) Horlait, D.; Lebreton, F.; Roussel, P.; Delahaye, T. XRD Monitoring of α Self-Irradiation in Uranium–Americium Mixed Oxides. *Inorg. Chem.* **2013**, *52* (24), 14196–14204.

(32) Horlait, D.; Caraballo, R.; Lebreton, F.; Jégou, C.; Roussel, P.; Delahaye, T. Self-Irradiation and Oxidation Effects on Americium Sesquioxide and Raman Spectroscopy Studies of Americium Oxides. *J. Solid State Chem.* **2014**, *217*, 159–168.

(33) Lebreton, F.; Martin, P. M.; Horlait, D.; Bès, R.; Scheinost, A. C.; Rossberg, A.; Delahaye, T.; Blanchart, P. New Insight into Self-Irradiation Effects on Local and Long-Range Structure of Uranium–Americium Mixed Oxides (through XAS and XRD). *Inorg. Chem.* **2014**, *53* (18), 9531–9540.

(34) Prieur, D.; Jankowiak, A.; Roudil, D.; Dubois, S.; Leorier, C.; Herlet, N.; Dehaudt, P.; Laval, J.-P.; Blanchart, P. Self-Irradiation Effects in Dense and Tailored Porosity U1–yAmyO2–x (y = 0.10; 0.15) Compounds. *J. Nucl. Mater.* **2011**, *411* (1–3), 15.

(35) Prieur, D.; Vigier, J.-F.; Wiss, T.; Janssen, A.; Rothe, J.; Cambriani, A.; Somers, J. Structural Investigation of Self-Irradiation Damaged AmO2. *J. Solid State Chem.* **2014**, *212*, 7–12.

(36) Scheinost, A. C.; Claussner, J.; Exner, J.; Feig, M.; Findeisen, S.; Hennig, C.; Kvashnina, K. O.; Naudet, D.; Prieur, D.; Rossberg, A.; Schmidt, M.; Qiu, C.; Colomp, P.; Cohen, C.; Dettona, E.; Dyadkin, V.; Stumpf, T. ROBL-II at ESRF: A Synchrotron Toolbox for Actinide Research. *J. Synchrotron Radiat.* **2021**, *28* (1), 333–349.

(37) Prieur, D.; Amidani, L.; Bazarkina, E. F.; Hennig, C.; Lawrence Bright, E.; Rossberg, A.; Silva, C. L.; Kvashnina, K. O. Frontiers of Synchrotron Methods for Actinide Science. *Chem.: Methods* **2025**, *5* (8), No. e202400073.

(38) Kvashnina, K. O.; Scheinost, A. C. A Johann-Type X-Ray Emission Spectrometer at the Rossendorf Beamline. *J. Synchrotron Radiat.* **2016**, *23* (3), 836–841.

(39) Ravel, B.; Newville, M. ATHENA, ARTEMIS, HEPHAESTUS: Data Analysis for X-Ray Absorption Spectroscopy Using IFEFFIT. *J. Synchrotron Radiat.* **2005**, *12* (4), 537–541.

(40) Joly, Y. X-Ray Absorption near-Edge Structure Calculations beyond the Muffin-Tin Approximation. *Phys. Rev. B* **2001**, *63* (12), No. 125120.

(41) Schindelin, J.; Arganda-Carreras, I.; Frise, E.; Kaynig, V.; Longair, M.; Pietzsch, T.; Preibisch, S.; Rueden, C.; Saalfeld, S.; Schmid, B.; Tinevez, J.-Y.; White, D. J.; Hartenstein, V.; Eliceiri, K.; Tomancak, P.; Cardona, A. Fiji: An Open-Source Platform for Biological-Image Analysis. *Nat. Methods* **2012**, *9* (7), 676–682.

(42) Kleykamp, H. The Chemical State of the Fission Products in Oxide Fuels. *J. Nucl. Mater.* **1985**, *131* (2), 221–246.

(43) Geiger, E.; Le Gall, C.; Gallais-During, A.; Pontillon, Y.; Lamontagne, J.; Hanus, E.; Ducros, G. Fission Products and Nuclear Fuel Behaviour under Severe Accident Conditions Part 2: Fuel Behaviour in the VERDON-1 Sample. *J. Nucl. Mater.* **2017**, *495*, 49–57.

(44) Kleykamp, H.; Paschoal, J. O.; Pejsa, R.; Thümmler, F. Composition and Structure of Fission Product Precipitates in Irradiated Oxide Fuels: Correlation with Phase Studies in the Mo-Ru-Rh-Pd and BaO-UO_2-ZrO_2-MoO_2 Systems. *J. Nucl. Mater.* **1985**, *130*, 426–433.

(45) Le Gall, C. Contribution à l'étude Du Relâchement Des Produits de Fission Hors de Combustibles Nucléaires En Situation d'accident Grave: Effet de la pO2 sur la Spéciation du Cs, Mo et Ba. Thèse de doctorat, Grenoble Alpes, 2018.

(46) Duriez, C.; Alessandri, J.-P.; Gervais, T.; Philipponneau, Y. Thermal Conductivity of Hypostoichiometric Low Pu Content (U,Pu)O_{2-x} Mixed Oxide. *J. Nucl. Mater.* **2000**, *277* (2–3), 143–158.

(47) Husainy, M.; Szenknect, S.; Podor, R.; Le Goff, X.; Kaczmarek, T.; Moisy, P.; Dacheux, N. Speciation and Chemical Behavior of Molybdenum in Uranium Dioxide Samples Prepared by Hydroxide Precipitation. *J. Nucl. Mater.* **2024**, *596*, No. 155075.

(48) Martin, P.; Ripert, M.; Carlot, G.; Parent, P.; Laffon, C. A Study of Molybdenum Behaviour in UO2 by X-Ray Absorption Spectroscopy. *J. Nucl. Mater.* **2004**, *326* (2), 132–143.

(49) Fouquet-Métivier, P.; Medyk, L.; Lebreton, F.; Guéneau, C.; Hunault, M. O. J. Y.; Solari, P.-L.; Dardenne, K.; Rothe, J.; Martin, P. M. Insight into the Cationic Charge Distribution in U1–y–ZPuyAmzO2 ± x Mixed Oxides. *Inorg. Chem.* **2024**, *63* (43), 20482–20491.

(50) Bazarkina, E. F.; Bauters, S.; Watier, Y.; Weiss, S.; Butorin, S. M.; Kvashnina, K. O. Exploring Cluster Formation in Uranium Oxidation Using High Resolution X-Ray Spectroscopy at Elevated Temperatures. *Commun. Mater.* **2025**, *6* (1), No. 75.

(51) Prieur, D.; Martel, L.; Vigier, J.-F.; Scheinost, A. C.; Kvashnina, K. O.; Somers, J.; Martin, P. M. Aliovalent Cation Substitution in UO_2: Electronic and Local Structures of $U_{1-y}La_yO_{2\pm x}$ Solid Solutions. *Inorg. Chem.* **2018**, *57*, 1535.

(52) Kvashnina, K. O. Electronic-Structure Interpretation: How Much Do We Understand Ce L3 XANES? *Chem. - Eur. J.* **2024**, *30* (46), No. e202400755.

(53) Martin, P.; Grandjean, S.; Valot, C.; Carlot, G.; Ripert, M.; Blanc, P.; Hennig, C. XAS Study of $(U_{1-y}Pu_y)O_2$ Solid Solutions. *J. Alloys Compd.* **2007**, *444–445*, 410–414.

(54) Vauchy, R.; Belin, R. C.; Robisson, A.-C.; Lebreton, F.; Aufore, L.; Scheinost, A. C.; Martin, P. M. Actinide Oxidation State and O/M Ratio in Hypostoichiometric Uranium–Plutonium–Americium $U_{0.750}Pu_{0.246}Am_{0.004}O_{2-x}$ Mixed Oxides. *Inorg. Chem.* **2016**, *55* (5), 2123–2132.

(55) Shannon, R. D.; Prewitt, C. T. Effective Ionic Radii in Oxides and Fluorides. *Acta Crystallogr., Sect. B:Struct. Sci.* **1969**, *25* (5), 925–946.

(56) Wauters, T. *Investigation of the Lattice Parameter and Sintering of Uranium Dioxide Doped with Zirconia and Gadolinia*; Faculty of Engineering Technology, Campus Groep T: Leuven, 2014.

(57) Sali, S. K.; Kulkarni, N. K.; Krishnan, K.; Achary, S. N.; Tyagi, A. K. Oxidation/Reduction Studies on $Zr_yU_{1-y}O_{2+x}$ and Delineation of a New Orthorhombic Phase in U–Zr–O System. *J. Solid State Chem.* **2008**, *181* (8), 1859–1866.

(58) Kleykamp, H. The Solubility of Selected Fission Products in UO_2 and (U, Pu)O_2. *J. Nucl. Mater.* **1993**, *206* (1), 82–86.

(59) Zhao, Y.; Weidner, D. J. Thermal Expansion of $SrZrO_3$ and $BaZrO_3$ Perovskites. *Phys. Chem. Miner.* **1991**, *18* (5), 294–301.

(60) Pauling, L. Atomic Radii and Interatomic Distances in Metals. *J. Am. Chem. Soc.* **1947**, *69* (3), 542–553.

(61) Kleykamp, H. Constitution and Thermodynamics of the Mo-Ru, Mo-Pd, Ru-Pd and Mo-Ru-Pd Systems. *J. Nucl. Mater.* **1989**, *167*, 49–63.

(62) Okamoto, H.; Massalski, T. B. The Au-Rh (Gold-Rhodium) System. *Bull. Alloy Phase Diagrams* **1984**, *5* (4), 384–387.

(63) Kleykamp, H. The Constitution of the Mo-Ru System. *J. Less-Common Met.* **1988**, *136* (2), 271–275.

(64) Arblaster, J. W. Crystallographic Properties of Palladium. *Platinum Met. Rev.* **2012**, *56* (3), 181–189.

(65) Singh, H. P. Determination of Thermal Expansion of Germanium, Rhodium and Iridium by X-Rays. *Acta Crystallogr., Sect. A: Found. Crystallogr.* **1968**, *24* (4), 469–471.

(66) Xing, H.; Hu, P.; Han, J.; Li, S.; Ge, S.; Hua, X.; Hu, B.; Yang, F.; Wang, K.; Feng, P. Effects of Oxygen on Microstructure and Evolution Mechanism of Body-Centred-Cubic Molybdenum. *Int. J. Refract. Met. Hard Mater.* **2022**, *103*, No. 105747.